The Indian Ocean Geoid Low at a plume-slab overpass

Bernhard Steinberger[a,b,*], Samurdhika Rathnayake[a,c], Elodie Kendall[a]

[a] GFZ German Research Centre for Geosciences, Telegrafenberg, 14473 Potsdam, Germany
[b] Centre for Earth Evolution and Dynamics, University of Oslo, PO Box 1028, 0315 Oslo, Norway
[c] Department of Land Surveying and Geo-Informatics, The Hong Kong Polytechnic University, 181 Chatham Road South, Kowloon, Hong Kong

Abstract

The Indian Ocean Geoid Low (IOGL) appears as a prominent feature if the geoid is, as usual, shown with respect to the Earth's reference shape. However, if it is shown relative to hydrostatic equilibrium, i.e. including excess flattening, it appears as merely a regional low on a north-south trending belt of low geoid. For a mantle viscosity structure with an increase of 2-3 orders of magnitude from asthenosphere to lower mantle, which is suitable to explain the long-wavelength geoid, a geoid low can result from both negative density anomalies in the upper mantle and positive anomalies in the lower mantle. Here we propose that the IOGL can be explained due to a linear, approximately north-south-trending high-density anomaly in the lower mantle, which is crossed by a linear, approximately West-Southwest - East-Northeast trending anomaly low-density anomaly in the upper mantle. While the former can be explained due to its location in a region of former subduction and inbetween the two Large Low Shear Velocity Provinces (LLSVPs), we propose here that the latter is due to an eastward outflow from the Kenya plume rising above the eastern edge of the African LLSVP. We show that, with realistic assumptions we can approximately match the size, shape and magnitude of the geoid low.

Keywords: geoid, slab, plume, Africa, India

1. Introduction

As most of the Earth's interior cannot be directly accessed, indirect evidence and/or modelling are generally used to constrain the mantle architecture. The geoid – the gravitational equipotential surface that most closely coincides with mean sea level – is a very high-quality dataset that contains information from the crust to the core. However, much of the longer-wavelength features of the geoid are unrelated to what is seen at the surface. This indicates that their origins lie deep in the Earth's interior. The Indian Ocean Geoid Low (IOGL) is one of the more prominent features, and therefore questions about its origin stay debated. To date, various sources which could give rise to the IOGL have been proposed in the literature, including a low-density anomaly in the upper mantle (Reiss et al., 2017; Rao et al., 2020) and high-density anomaly in the lower mantle (Rao and Kumar, 2014), as both can cause a geoid low. Recently, Ghosh et al. (2017) have shown that the IOGL can be explained well by mantle density anomalies inferred from seismic tomography, but the cause of these density anomalies was not thoroughly investigated.

The IOGL becomes very prominent if one considers the geoid as the deviation of an equipotential surface from the reference spheroid, which is slightly more flattened than the Earth's equilibrium shape (Figure

*Corresponding author; e-mail: bstein@gfz-potsdam.de, phone: +49-331-288-1881

1, left). Accordingly, a geoid with respect to the hydrostatic equilibrium shape (second from left), which includes excess flattening, shows a local minimum along a belt stretching from the Antarctic to Arctic. Hence, plotting the geoid with respect to the reference ellipsoid, as is often done, promotes a biased view overemphasizing the importance of certain features including the IOGL, but also a geoid high over Iceland. After additionally correcting for the crust, which mostly has an effect around Tibet, the IOGL appears even more connected to the geoid low under Asia (third from left). The right panel also corrects for the isostatically compensated sea floor depth variations with ocean age. If one further corrects for the effects of upper mantle slabs (Hager, 1984, not shown here), which, in this hemisphere, mainly reduces the geoid height in a region stretching from New Guinea through Indonesia to Japan, the remaining "residual" geoid shows a higher correlation with the Large Low Shear Velocity Provinces (LLSVPs). Accordingly, the dominating large-scale structure of the residual geoid, including the roughly NNW-SSE trending trough between the LLSVPs, can be well-explained from lower-mantle density anomalies inferred from seismic tomography (Hager and Richards, 1989).

But this does not explain the IOGL as a feature superposed on this large-scale trough. The idea of the presence of a thermal anomaly in the upper mantle has been suggested (Reiss et al., 2017; Ghosh et al., 2017; Rao et al., 2020) to explain the origin of this geoid anomaly. However, where could the proposed hot anomaly originate from? To address this question, Nerlich et al. (2016) produced forward models of mantle flow constrained by surface plate motion. They found a good match for one particular plate reconstruction, due to the combination of hot plume material in the upper mantle that has been dragged northward by the fast-moving India plate, and cold slab material in the mantle beneath. Spasojevic et al. (2010) concluded that the long-wavelength trough in the geoid is linked to high-density slab graveyards in the lower mantle, whereas upwelling regions in the mantle above 1,000 km depth cause discrete lows within the larger trough. They suggest that this mode of upwelling in the mid-to-upper mantle is caused by buoyant hydrated mantle that was created by processes around and above subducted slabs. Here, we consider another different scenario: The IOGL is elongated towards East Africa, and it could be correlated with an outflow from the Kenya plume rising from the margin of the African LLSVP, as imaged by recent tomography models (Chang et al., 2020, 2015; Durand et al., 2017; Boyce et al., 2021). As the LLSVP margin is overlain by many plumes, and by many reconstructed eruption locations of Large Igneous Provinces (LIPs) it has been proposed to be a "Plume Generation Zone" (Burke et al., 2008). Evidence for a hot midmantle anomaly in the area of the IOGL has also been reported by Reiss et al. (2017) who used the differential travel times of PP, SS waves and their precursors. Additionally, Rao et al. (2020) map a thin mantle transition zone from 3-D time to depth migration of P receiver functions.

In this study, we aim at integrating these various suggestions and concepts into a common mantle dynamic framework. We pursue the idea stemming from Ghosh et al. (2017) that the IOGL occurs at the crossing point of a roughly north-south trending positive anomaly in the lower mantle (e.g. slabs from the "ring of fire") and a roughly East-West to WSW-ENE trending negative anomaly in the upper mantle by developing a set of simple, synthetic geoid/density models, based on a viscous flow modeling approach, as is appropriate for the sublithospheric mantle. With this method we can constrain which parameters such as the width and depth extent of density anomalies lead to a geoid that matches observations and we will discuss how our proposed scenario is supported by a number of other observations.

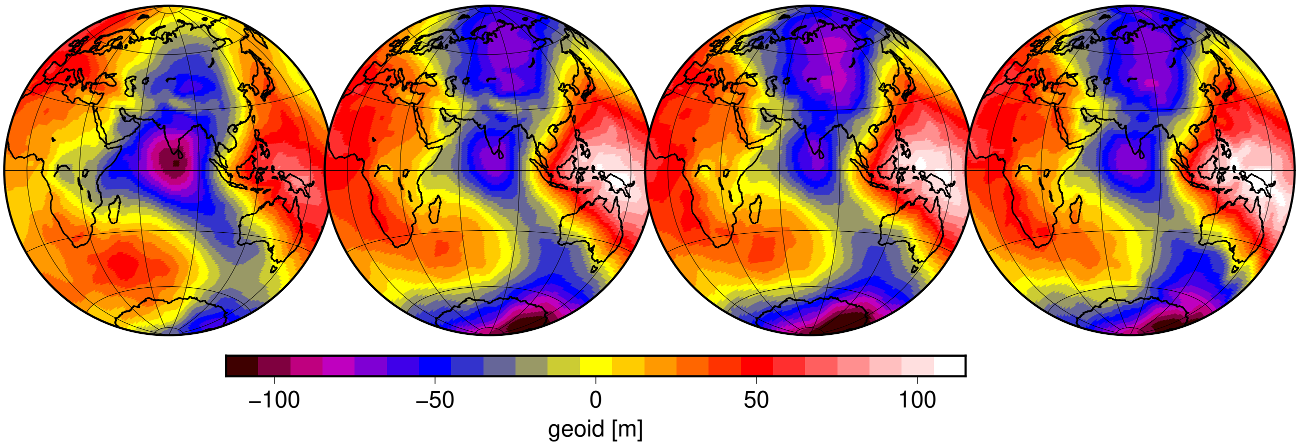

Figure 1: Observed geoid (Pavlis et al., 2012) from left to right (i) relative to reference shape, i.e. disregarding excess flattening (ii) relative to equilibrium spheroid (Nakiboglu, 1982) (iii) minus contribution down to the base of the crust derived from CRUST1.0 (Laske et al., 2013), and (iv) minus the effect of ocean floor age (Müller et al., 2008) following Steinberger (2016) and assuming isostatic compensation. The geoid is expanded to spherical harmonic degree 63, with a spectral cosine taper in the degree range 32-63.

2. Methodology

Our geoid computations are based on a spherical harmonic expansion of mantle densities. If one assumes a viscous rheology with radial viscosity variations only, both the flow field (Hager and O'Connell, 1979, 1981) and the geoid can be computed separately for each spherical harmonic degree and order. Expansion coefficients of the geoid can be computed by multiplying, at each depth, expansion coefficients of density with a depth-dependent geoid kernel (Richards and Hager, 1984; Ricard et al., 1984), integrating over depth and multiplying with a pre-factor that only depends on spherical harmonic degree. Figure 2 shows that these kernels reverse sign in the lower mantle, particularly for long wavelengths ($\sim$degree 2-5). In this way, a positive density anomaly in the lower part of the mantle, and a negative density anomaly closer to the surface can give rise to a negative geoid. For shorter wavelengths (degrees 6 and higher), the lower part of the mantle has a smaller contribution to the observed geoid, and a negative geoid can result from both negative density anomaliles at intermediate depths (below $\sim$200-300 km) and a positive anomaly at shallower depths. The combined effect of density anomalies of different sizes and at various depth on the geoid is not straightforward and it is therefore important to consider some simple synthetic density models to assess the dependence of the geoid on these various parameters.

The geoid kernels consider both the effect of the mantle density anomalies and the dynamic topography (i.e. uplift related to negative anomalies at the surface and core-mantle boundary) that are caused by mantle flow driven by those density anomalies. Depending on whether, at a given depth and spherical harmonic degree, the geoid contribution of the density anomalies themselves, or the contribution of dynamic topography is larger, the kernel is positive or negative. If lateral viscosity variations (LVVs) are considered (Ghosh et al., 2010, 2017) the kernel approach cannot be used, and one can instead directly use the numerically computed dynamic topography. Alternatively, it is also possible to use observation-based residual topography (Kaban et al., 1999), but this is not applicable for our approach using synthetic density models. Since Ghosh et al. (2010) substantiate that the geoid calculated from tomography is hardly affected by the presence of LVVs, we conclude that this is also the case for our synthetic models, which are characterized by a similarly long wavelength. They also find that by taking into account LVVs, the geoid with appropriate surface velocity boundary conditions agrees with free slip cases. We therefore consider it adequate to use the kernel approach with only radial viscosity variations, a free-slip surface boundary condition, an effective lithosphere viscosity, and synthetic density anomalies based on tomography, which has been shown to yield a good fit to the geoid globally (Steinberger, 2016). We also find the kernel approach more illustrative, and it is computationally less intensive than the alternative method considering LVVs.

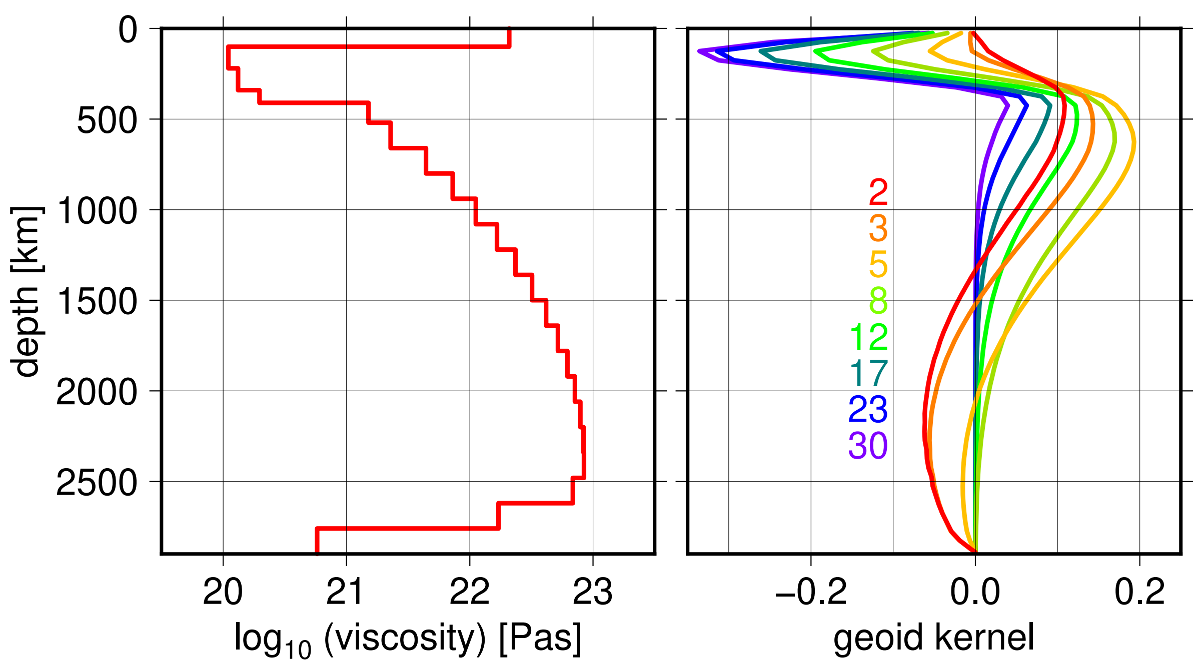

Figure 2: Left: reference viscosity structure from Steinberger (2016). Right: corresponding geoid kernels for spherical harmonic degrees 2, 3, 5, 8, 12, 17, 23, 30.

For density anomalies, we consider a high-density "ring" in the lower mantle and a low-density "streak" in the upper mantle. In order to avoid sharp edges which, after spherical harmonic expansion, can lead to "ringing", i.e. artificial small-scale fluctuations, we smooth these features with a cosine taper, i.e. for a width w and a maximum value ρ_0 the density anomaly as a function of distance x from the center line smoothly varies as $\rho(x) = \rho_0 \cdot (0.5 + 0.5\cos(\pi x/w))$ for $|x| < w$ and is zero for $|x| \geq w$. For example, a half-width $w/2$ =7 degrees means the density anomaly has gradually dropped to half the centerline value at 7 degrees from the centerline, and to zero at 14 degrees from it. Additionally, we apply a spectral cosine taper in the degree range 32-63 after expanding these features in spherical harmonics until degree and order 63, to further prevent possible ringing.

3. Results

Figure 3 shows one representative result. The geoid is caused by a high-density "ring" in the lower mantle (half-width 15 degrees, depth extent 1500-2600 km, $\sim$ north - south, all around the Earth, along a great circle) and a low-density "streak" in the upper mantle (half-width 7 degrees, 100-400 km depth extent) from East Africa (30°E, where there is a large upwelling from the African LLSVP) towards East-Northeast until 120°E near the subduction zones. An upper mantle density anomaly of -0.7% corresponds to a thermal expansivity of $2.8 \cdot 10^{-5}$/K, which is approximately appropriate for the 100-400 km depth range (Steinberger and Calderwood, 2006; Schmeling et al., 2003) combined with a plume temperature anomaly of 250 K, corresponding to generic estimates (Schubert et al., 2001). With the phase boundary parameters chosen (Steinberger, 2007) the full effect of the olivine-spinel phase transition corresponds to doubling the density anomaly for a 138 km thick layer. Corresponding to 125 K temperature anomaly at the depth of the phase transition, half of the effect is included in Figure 3. It is assigned to the 350-400 km depth layer, i.e. at 375 km depth. Each of these density anomalies in the upper and lower mantle, when considered separately, results in an elongated geoid anomaly; the roughly circular anomaly can only be obtained with a combination of both.

The modelled geoid built with these parameters (Figure 3) reproduces the overall size and shape of the actual geoid low of $\sim$30 m (relative to the "saddle" to the north) or $\sim$50 m (relative to the "saddle" to the SE), on an extended roughly north-south trending geoid low well. We consider this our best-fit model, though the fit was only assessed qualitatively. The main purpose of this figure is to illustrate how the shape of the anomaly (shown in map view) can be obtained by a combination of two anomalies (shown in cross section). We consider one map view (an additional one is included in the supplement) sufficient for this purpose, because we think that the reader can now picture the maps resulting by combining any two profiles described in the following paragraph quite easily.

The dependence of the geoid on the size and depth range of the anomaly is illustrated in Figure 4. In this way, model uncertainties due to uncertain densities can be assessed. Here we consider high-density anomalies in the lower mantle and low-density anomalies in the upper mantle separately. To understand the resulting geoid, one has to consider that a low density anomaly by itself always causes a geoid low, but the resulting dynamic topography highs, both at the surface and core-mantle boundary (the latter playing a smaller role and being negligible for upper-mantle anomalies) cause a geoid high. The opposite is the case for high density anomalies. Because the respective low and high can have different width, with their relative width depending on viscosity structure, a rather complicated total anomaly, with a narrower high overlaying a wider low, can result. We also investigated the effect of partially (50 %) or fully including the equilibrium effect of the olivine-spinel phase transition.

For the low-density streak in the upper mantle, the geoid low is always surrounded by a larger, less prominent geoid high. This occurs because by definition there cannot be a degree-one geoid, implying a

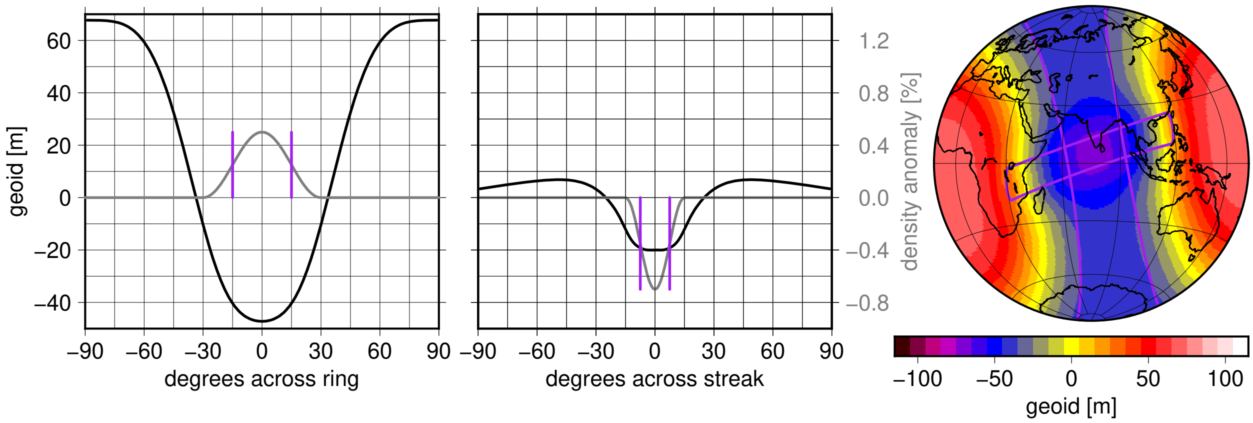

Figure 3: Modelled geoid profiles and map. Left: Effect of a a high-density "ring" in the depth range 1500 km to 2600 km (grey line; axis labels on the right of center panel) on geoid height (black line). Center: Effect of a low-density "streak" in the depth range 100 km to 400 km (grey line) on geoid height along a profile orthogonal to the streak across its centerpoint. 50 % of the effect of the olivine-spinel phase transition is also considered. Right: Map view of the geoid from the density anomalies of the other two panels combined. The centerline of the ring follows a great circle with a pole at 10°S, 12°W. The streak extends from 30°E to 120°E and its centerline follows a great circle with a pole at 70°N, 30°W. Purple lines show the outlines of the surface projection of both the ring and the streak, where each anomaly is at 50% of its maximum, corresponding to the vertical purple lines in the left and center panels.

compensating geoid high on the same hemisphere. In some cases, there is also a narrow central local geoid high, caused by the effect of dynamic topography. The narrower geoid high (Figure 4) appears, relatively, most prominently for a comparatively thin streak and in cases where the anomaly is restricted to shallow depth. The fact that the actual geoid low does not feature a central high could indicate that the density anomaly is more prominent near the transition zone, as suggested in previous work (Reiss et al., 2017; Rao et al., 2020). The exothermic phase transition at around a depth of 410 km may further strengthen the effect of any temperature and density anomalies around that depth.

The width of the geoid low also depends on the width of the streak, albeit not proportionally: For example, for a narrow streak (e.g. 3 degrees half-width) the width of the geoid low can be much wider, with still about half the maximum value around 12 degrees from the center line. On the other hand, a wider streak gives rise to a geoid low of higher amplitude, but only slightly wider. We report that, for a realistic range of parameters, the modelled geoid amplitude ($\sim$30 m) matches the observed geoid well.

For the positive, lower mantle density anomaly, a narrower, central geoid high may occur due to the effect of the density anomaly itself. This high is more prominent for shallower anomalies, and for narrower rings. It does not occur if density anomalies are restricted to depths below 1800 km. The width of this geoid low is almost independent of the width of the high-density ring. Instead, the anomaly width almost only maps into the amplitude of the geoid low, with half the maximum value around 30 to 40 degrees from the center line. This can be explained because, for an anomaly in the mantle below 1000 km, the resulting topography low is dominated by the very longest wavelengths, regardless of the size of the anomaly itself.

4. Discussion

The highest mantle viscosity likely lies in the depth range 1500–2600 km (Steinberger, 2016). At these depths, sinking rates reach a minimum and hence this region hosts most slabs. Slabs would also accumulate in the lowermost mantle, but there are indications that thermochemical piles also reside in the lowermost mantle with a positive density anomaly (Lau et al., 2017). Hence we also consider cases in Figures 3 and 4 where the density anomaly does not reach the bottom of the mantle, because it is not clear whether piles or slabs have a higher density in the lowermost mantle. Also, the density contrast between ring and elsewhere may be due to density contrast between slab and ambient mantle, but also between hot material rising above LLSVPs and average mantle. The latter would presumably correspond to a wider ring. A depth range of 100 to 400 km for the upper mantle streak corresponds to the sublithospheric upper mantle, where the viscosity-depth profile is likely at a minimum (Steinberger, 2016). If the hot plume material is mainly fed to the mantle above the olivine-spinel phase transition, the temperature anomaly at the phase transition may be less than the average anomaly in the upper mantle. In order to account for this uncertainty, we consider the effect of the phase transition either fully, half or not at all.

Current tomography models that can fit the IOGL show low velocity anomalies in the depth range of 300-900 km as also shown by Ghosh et al. (2017) (see also Figure 5). In Figure S1 we show that also for this depth range, with a lower density anomaly of 0.2% the size and shape of the IOGL can be approximately fit.

To further assess whether this conceptual model could be realistic, we show in Figure 6 present-day mantle flow and average density in the upper mantle for the reference model of Steinberger (2016). That is, the computational method is the same as for the synthetic models described above, however, surface plate motions (instead of free-slip) are prescribed as boundary conditions, and density is instead based on a combination of two tomography models – SL2013SV (Schaeffer and Lebedev, 2013) closer to the surface and a recent update of Grand (2002) deeper down, with a transition at 200 km depth, as the resolution of SL2013SV deteriorates at larger depth. Seismic velocity anomalies are converted to density anomalies with a depth-dependent factor that is derived from mineral physics, except in the continental lithosphere shallower than 150 km, where we instead use a small constant density anomaly of 0.2%. More details, such as which volumes are treated as continental lithosphere, are given in Steinberger (2016). This density field is given at specific depth levels, where also velocity is evaluated. We use the same radial viscosity structure as in Figure 2. To plot velocity, the 262.5 km depth level was chosen, as for the viscosity structure used it is approximately in the middle of the asthenospheric low-viscosity channel, where the plume material will flow. But it is also likely below the thickest lithosphere (e. g. Globig et al., 2016; Steinberger, 2016), therefore entirely within the asthenosphere, and hence computed flow speeds are realistic. It shows a series of low density material which, in combination with the arrows showing horizonal flow (10 degrees of arc arrow length = 5 cm/yr) could indicate an ENE outflow from the Kenya plume towards the southern tip of India. This is further visualized by a cross section through the same density and flow model (Figure 5).

This low density anomaly correlates well with a linear low S-velocity anomaly east of East Africa, extending from north of Madagascar northeastward towards the west coast of India, as shown in red/orange colors in the votemap (Hosseini et al., 2018; Shephard et al., 2017) in Figure 7 which combines many tomographic models. The geometry of this low S-wave anomaly should be resolvable as most current global tomography models have a nominal lateral resolution of ∼1000 km. A flow field into the upper mantle beneath East Africa and in the upper mantle laterally away from the LLSVP is a persistent and robust feature of many models. Isosurfaces of low-velocity anomalies in current global tomography models such as SGLOBE-rani (Chang et al., 2015), SAVANI (Auer et al., 2014), SEISGLOB2 (Durand et al., 2017) and S362ANI (Kustowski et al., 2008) indicate that hot material may flow east to north-eastward from Kenya towards the mid-oceanic ridge and south of India (Figure S2).

The pattern of density anomalies and flow field in Figure 6 indicates that the connection between the African superplume or Kenya plume and the Indian Ocean would be just north of Madagascar. Figures 6 and 7 suggest there is a region of thicker lithosphere beneath the Horn of Africa (Somalia), however, south of it and north of Madagascar there could be a "channel" for material to flow eastward towards the Indian Ocean. Maps of lithospheric thickness beneath Africa from elevation, geoid and thermal analysis (Figure 8 in Globig et al., 2016) also show a region of thicker lithosphere northeast of Kenya, beneath the Horn of Africa. Lithosphere thickness in this region could be around 160–200 km (Globig et al., 2016; Steinberger, 2016). However, there are considerable uncertainties associated with these lithospheric thickness estimates. For example, other models based in part on tomography (e.g. Afonso et al., 2019) as well as the thermal model of Artemieva (2006) suggest that the lithospheric thickness is only around 100 km. Models also indicate thicker lithosphere west of Kenya, for the Congo Craton. Flow may be diverted around regions of thick lithosphere and focussed in regions of thinner lithosphere, corresponding to the concept of upside down drainage (Sleep, 1997). The channeled flow eastward from the Kenya plume could be similar to the one proposed from the Afar plume towards the Gulf of Aden and a northward channel towards Arabia (e.g., Chang and Van der Lee, 2011; Chang et al., 2011).

Mantle plumes can tilt due to plate motion and/or mantle wind (e.g., Skilbeck and Whitehead, 1978; Olson and Singer, 1985). Following the geodynamic modelling studies of plumes with and without the presence of mantle wind (Steinberger and Antretter, 2006; Richards and Griffiths, 1988) and with plate-like behaviour (e.g., Arnould et al., 2020), Davaille et al. (2005) and Chang et al. (2020) concluded it to be impossible to link the low velocity anomaly beneath South Africa to that beneath Afar (tilt ∼45 degrees). As the IOGL is further from South Africa than Afar, we find it more plausible that material is channeled in the upper manntle from the Kenya plume. However, in order to plausibly explain the size of the anomaly, it is necessary that, in the IOGL area the material not only occurs at the base of the lithosphere but reaches at least to 410 km depth. This could possibly be due to a downward pull induced by subducted slabs in the lower mantle.

This flow from the Kenya plume towards the IOGL would be part of a larger-scale "conveyor belt" (Becker and Faccenna, 2011) from an upwelling associated with the African LLSVP towards the Tethyan collisional belt with its subducted slabs. A transition from eastward towards more northeastward flow further east could be due to the strong northward component of the Indian plate motion dragging material along (Ghosh et al., 2017). This is in accord with observations of azimuthal anisotropy, which often show a change in fast orientation from ENE beneath the African plate northeast of Madagascar to NNE beneath the Indian plate. For example, this can be seen clearly for the model SL2016svAr of Schaeffer et al. (2016) at depth 110-200 km, but also for the model 3D2015-07Sva of Debayle et al. (2016) at a similar depth range, and Yuan and Beghein (2013) at $\sim$ 150-300 km depth.

The Kenya plume originates around 45 Ma as an upper bound (Ebinger et al., 1993; Nelson et al., 2012). With typical flow speeds of roughly about 5 cm/yr this would then correspond to 2250 km total flow, which is not quite enough to reach the IOGL. But of course, flow speeds are uncertain and might also be faster, in particular for hot and low-viscosity plume material - this computation doesn't consider lateral viscosity variations. With an approximate great circle distance (at depth 262.5 km) of 4500 km between the Kenya plume and the IOGL a speed of at least $\approx$ 10 cm/yr, i.e. twice as high, would be required for plume material to reach the IOGL within 45 Myr.

Another possible source of hot material below the IOGL is from the Réunion plume (Ghosh et al., 2017). This plume is older (around 65 Ma) and closer to the IOGL, and it was initially located beneath the Indian plate, which could have aided in dragging hot material along. However, mantle flow streamlines from La Réunion (Figure 6) end up further south. In light of this and because the IOGL has an extension towards East Africa, we consider the Kenya plume a more likely source.

For the results shown in this paper, we only consider one specific viscosity model (Figure 2), but mantle viscosity structure is uncertain with a wide variety of models recently proposed. We consider it sufficient for our purpose, though, to use a viscosity model that is suitable to explain the global geoid (Steinberger, 2016). In this case, the geoid predicted based on the synthetic density models used here can also be considered realisitic. Obviously, with an otherwise poorly constrained viscosity model we cannot tightly constrain the density models responsible for the geoid low. Our goal is merely to propose a model that is dynamically reasonable and not in obvious conflict with other evidence. Also, for a more thorough investigation, other observations, and not just the geoid, should also be considered.

5. Conclusions

Building upon previous ideas we show that a nearly circular geoid low in the Indian Ocean can be the result of the superposition of two nearly orthogonal geoid troughs, one due to slabs in the lower mantle and the other geoid trough due to hot material in the upper mantle. By constructing synthetic density models with realistic assumptions, we show that the size, shape and amplitude of the IOGL can all be matched well. We have assessed uncertainties in the density models by varying several parameters. However, our main purpose is to show that our model can give an explanation of the IOGL with realistic assumptions, not a thorough discussion of uncertainties. Accordingly, we only use one viscosity model varying only with radius, which has previously been shown to be adequate for modelling the geoid and allow a good fit globally.

We propose an origin of the hot material from an upwelling plume from the eastern margin of the African LLSVP. Large-scale global flow models indicate that material flows from the LLSVP towards the upper mantle beneath East Africa and then is possibly channeled further in an east/north-easterly direction towards the South of India. Dynamical models also suggest that a strong tilt of the plume itself, towards the IOGL, is unlikely, and that flow rather follows the base of the lithosphere. We regard the Kenya plume as the most likely candidate for the origin of the hot material. This plume has recently been imaged as a feature separate from the Afar plume, at least in the upper mantle, rising from the African LLSVP. Since the Afar plume likely feeds into the rifts of the Red Sea and Gulf of Aden, material from the Kenya plume would have to feed elsewhere. Flow from the Kenya plume is likely to be partially obstructed by blocks of thick lithosphere, especially around the Horn of Africa. Yet there appears to be comparatively thin lithosphere south of it, and north of Madagascar, where outflow towards the East could occur. Such an outflow, and continuously hot material towards the IOGL is also evidenced by seismic tomography.

Acknowledgements

This work was partially funded by the Research Council of Norway Centre of Excellence Project 223272. Additional funding was provided from the innovation pool of the Helmholtz Association through the Advanced Earth System Modelling Capacity (ESM) activity. We thank two reviewers for their thorough and constructive comments which helped to considerably clarify many issues.

References

Afonso, J.C., Salajegheh, F., Szwillus, W., Ebbing, J., Gaina, C., 2019. A global reference model of the lithosphere and upper mantle from joint inversion and analysis of multiple data sets. Geophys. J. Int. 217, 1602–1628. doi:10.1093/gji/ggz094.

Arnould, M., Coltice, N., Flament, N., Mallard, C., 2020. Plate tectonics and mantle control on plume dynamics. Earth Planet. Sci. Lett. 547, 116439. doi:10.1016/j.epsl.2020.116439.

Artemieva, I.M., 2006. Global $1° \times 1°$ thermal model TC1 for the continental lithosphere: Implications for lithosphere secular evolution. Tectonophys. 416, 245–277. doi:10.1016/j.tecto.2005.11.022.

Auer, L., Boschi, L., Becker, T.W., Nissen-Meyer, T., Giardini, D., 2014. Savani: A variable resolution whole-mantle model of anisotropic shear velocity variations based on multiple data sets. J. Geophys. Res. - Sol. Ea. 119, 3006–3034. doi:10.1002/2013JB010773.

Becker, T.W., Faccenna, C., 2011. Mantle conveyor beneath the Tethyan collisional belt. Earth Planet. Sci. Lett. 310, 453–461. doi:10.1016/j.epsl.2011.08.021.

Boyce, A., Bastow, I.D., Cottaar, S., Kounoudis, R., De Courbeville, J.G., Caunt, E., Desai, S., 2021. AFRP20: New P-wavespeed model for the African mantle reveals two whole-mantle plumes below East Africa and Neoproterozoic modification of the Tanzania craton. Geochem., Geophys., Geosys. 22, e2020GC009302. doi:10.1029/2020GC009302.

Burke, K., Steinberger, B., Torsvik, T.H., Smethurst, M.A., 2008. Plume Generation Zones at the margins of Large Low Shear Velocity Provinces on the the core-mantle boundary. Earth Planet. Sci. Lett. 265, 49–60. doi:10.1016/j.epsl.2007.09.042.

Chang, S.J., Ferreira, A.M.G., Ritsema, J., van Heijst, H.J., Woodhouse, J.H., 2015. Joint inversion for global isotropic and radially anisotropic mantle structure including crustal thickness perturbations. J. Geophys. Res. - Sol. Ea. 120, 4278–4300. doi:10.1002/2014JB011824.

Chang, S.J., Kendall, E., Davaille, A., Ferreira, A.M.G., 2020. The evolution of mantle plumes in East Africa. J. Geophys. Res. - Sol. Ea. 125, e2020JB019929. doi:10.1029/2020JB019929.

Chang, S.J., Van der Lee, S., 2011. Mantle plumes and associated flow beneath Arabia and East Africa. Earth Planet. Sci. Lett. 302, 448–454. doi:10.1016/j.epsl.2010.12.050.

Chang, S.J., Merino, M., Van der Lee, S., Stein, S., Stein, C.A., 2011. Mantle flow beneath Arabia offset from the opening Red Sea. Geophys. Res. Lett. 38, L04301. doi:10.1029/2010GL045852.

Davaille, A., Stutzmann, E., Silveira, G., Besse, J., Courtillot, V., 2005. Convective patterns under the Indo-Atlantic box. Earth Planet. Sci. Lett. 239, 233–252. doi:10.1016/j.epsl.2005.07.024.

Debayle, E., Dubuffet, F., Durand, S., 2016. An automatically updated s-wavemodel of the upper mantle and the depth extent of azimuthal anisotropy. Geophys. Res. Lett. 43, 674–682. doi:10.1002/2015GL067329.

Durand, S., Debayle, E., Ricard, Y., Zaroli, C., Lambotte, S., 2017. Confirmation of a change in the global shear velocity pattern at around 1000 km depth. Geophys. J. Int. 211, 1628–1639. doi:10.1093/gji/ggx405.

Ebinger, C.J., Yemane, T., Woldegabriel, G., Aronson, J.L., Walter, R.C., 1993. Late Eocene-recent volcanism and faulting in the southern main Ethiopian rift. J. Geol. Soc. London 150, 99–108. doi:10.1144/gsjgs.150.1.0099.

Ghosh, A., Becker, T.W., Zhong, S.J., 2010. Effects of lateral viscosity variations on the geoid. Geophys. Res. Lett. 37, L01301. doi:10.1029/2009GL040426.

Ghosh, A., Thyagarajulu, G., Steinberger, B., 2017. The importance of upper mantle heterogeneity in generating the Indian Ocean geoid low. Geophys. Res. Lett. 44, 9707–9715. doi:10.1002/2017GL075392.

Globig, J., Fernndez, M., Torne, M., Vergs, J., Robert, A., Faccenna, C., 2016. New insights into the crust and lithospheric mantle structure of Africa from elevation, geoid, and thermal analysis. J. Geophys. Res. - Sol. Ea. 121, 5389–5424. doi:10.1002/2016JB012972.

Grand, S.P., 2002. Mantle shear-wave tomography and the fate of subducted slabs. Phil. Trans. R. Soc. Lond. A 360, 2475–2491. doi:10.1098/rsta.2002.1077.

Hager, B.H., 1984. Subducted slabs and the geoid: constraints on mantle rheology and flow. J. Geophys. Res. 89, 6003–6015.

Hager, B.H., O'Connell, R.J., 1979. Kinematic models of large-scale flow in the Earth's mantle. J. Geophys. Res. 84, 1031–1048. doi:10.1029/JB084iB03p01031.

Hager, B.H., O'Connell, R.J., 1981. A simple global model of plate dynamics and mantle convection. J. Geophys. Res. 86, 4843–4867. doi:10.1029/JB086iB06p04843.

Hager, B.H., Richards, M.A., 1989. Long-wavelength variations in Earth's geoid: physical models and dynamical implications. Philosophical Transactions of the Royal Society of London. Series A, Mathematical and Physical Sciences 328, 309–327. doi:10.1098/rsta.1989.0038.

Hosseini, K., Matthews, K.J., Sigloch, K., Shephard, G.E., Domeier, M., Tsekhmistrenko, M., 2018. SubMachine: Web-Based tools for exploring seismic tomography and other models of Earth's deep interior. Geochem., Geophys., Geosys. 19, 1464–1483. doi:10.1029/2018GC007431.

Kaban, M.K., Schwintzer, P., Tikhotsky, S.A., 1999. A global isostatic gravity model of the Earth. Geophys. J. Int. 136, 519–536. doi:10.1046/j.1365-246x.1999.00731.x.

Laske, G., Masters., G., Ma, Z., Pasyanos, M., 2013. Update on CRUST1.0 - a 1-degree global model of Earth's crust. Geophys. Res. Abstr. 15. Abstract EGU2013-2658.

Lau, H., Mitrovica, J.X., Davis, J.L., Tromp, J., Yang, H.Y., Al-Attar, D., 2017. Tidal tomography constrains Earths deep-mantle buoyancy. Nature 551, 321–326. doi:10.1038/nature24452.

Müller, R.D., Sdrolias, M., Gaina, C., Roest, W.R., 2008. Age, spreading rates, and spreading asymmetry of the world's ocean crust. Geochem., Geophys., Geosys. 9, Q04006. doi:10.1029/2007GC001743.

Nakiboglu, S.M., 1982. Hydrostatic theory of the Earth and its mechanical implications. Phys. Earth Planet. Inter. 28, 302–311. doi:10.1016/0031-9201(82)90087-5.

Nelson, W.R., Furman, T., van Keken, P.E., Shirey, S.B., Hanan, B.B., 2012. Os-Hf isotopic insight into mantle plume dynamics beneath the East African Rift system. Chem. Geol. 320-321, 66–79. doi:10.1016/j.chemgeo.2012.05.020.

Nerlich, R., Colli, L., Ghelichkhan, S., Schuberth, B., Bunge, H.P., 2016. Constraining central Neo-Tethys Ocean reconstructions with mantle convection models. Geophys. Res. Lett. 43, 9595–9603. doi:10.1002/2016GL070524.

Olson, P., Singer, H., 1985. Creeping plumes. J. Fluid Mech. 158, 511–531. doi:10.1017/s0022112085002749.

Pavlis, N.K., Holmes, S.A., Kenyon, S.C., Factor, J.K., 2012. The development and evaluation of the Earth Gravitational Model 2008 (EGM2008). J. Geophys. Res. 117, B04406. doi:10.1029/2011JB008916.

Rao, B.P., Kumar, M.R., 2014. Seismic evidence for slab graveyards atop the Core Mantle Boundary beneath the Indian Ocean Geoid Low. Phys. Earth Planet. Inter. 236, 52–59. doi:10.1016/j.pepi.2014.08.005.

Rao, B.P., Kumar, M.R., Saikia, D., 2020. Seismic evidence for a hot mantle transition zone beneath the Indian Ocean Geoid Low. Geochem., Geophys., Geosys. 21, e2020GC009079. doi:10.1029/2020GC009079.

Reiss, A.S., Thomas, C., van Driel, J., Heyn, B., 2017. A hot midmantle anomaly in the area of the Indian Ocean Geoid Low. Geophys. Res. Lett. 44, 6702–6711. doi:10.1002/2017GL073440.

Ricard, Y., Fleitout, L., Froidevaux, C., 1984. Geoid heights and lithospheric stresses for a dynamic Earth. Ann. Geophys. 2, 267–286.

Richards, M.A., Griffiths, R.W., 1988. Deflection of plumes by mantle shear flow: Experimental results and a simple theory. Geophys. J. 94, 367–376. doi:10.1111/j.1365-246x.1988.tb02260.x.

Richards, M.A., Hager, B.H., 1984. Geoid anomalies in a dynamic Earth. J. Geophys. Res. 89, 5987–6002. doi:10.1029/JB089iB07p05987.

Schaeffer, A., Lebedev, S., 2013. Global shear speed structure of the upper mantle and transition zone. Geophys. J. Int. 194, 417–449. doi:10.1093/gji/ggt095.

Schaeffer, A., Lebedev, S., Becker, T., 2016. Azimuthal seismic anisotropy in the earth's upper mantle and the thickness of tectonic plates. Geophys. J. Int. 207, 901–933. doi:10.1093/gji/ggw309.

Schmeling, H., Marquart, G., Ruedas, T., 2003. Pressure- and temperature-dependent thermal expansivity and the effect on mantle convection and surface observables. Geophys. J. Int. 154, 224–229. doi:10.1046/j.1365-246X.2003.01949.x.

Schubert, G., Turcotte, D.L., Olson, P., 2001. Mantle Convection in the Earth and Planets. Cambridge University Press.

Shephard, G.E., Matthews, K.J., Hosseini, K., Domeier, M., 2017. On the consistency of seismically imaged lower mantle slabs. Scientific Reports 7, 10976. doi:10.1038/s41598-017-11039-w.

Skilbeck, J.N., Whitehead, J.A.J., 1978. Formation of discrete islands in linear island chains. Nature 272, 499–501. doi:10.1038/272499a0.

Sleep, N.H., 1997. Lateral flow and ponding of starting plume material. J. Geophys. Res. - Sol. Ea. 102, 10001–10012. doi:10.1029/97JB00551.

Spasojevic, S., Gurnis, M., Sutherland, R., 2010. Mantle upwellings above slab graveyards linked to the global geoid lows. Nat. Geosci. 3, 435–438. doi:10.1038/ngeo855.

Steinberger, B., 2007. Effect of latent heat release at phase boundaries on flow in the Earth's mantle, phase boundary topography and dynamic topography at the Earth's surface. Phys. Earth Planet. Inter. 164, 2–20. doi:10.1016/j.pepi.2007.04.021.

Steinberger, B., 2016. Topography caused by mantle density variations: observation-based estimates and models derived from tomography and lithosphere thickness. Geophys. J. Int. 205, 604–621. doi:10.1093/gji/ggw040.

Steinberger, B., Antretter, M., 2006. Conduit diameter and buoyant rising speed of mantle plumes: Implications for the motion of hot spots and shape of plume conduits. Geochem., Geophys., Geosys. 7, Q11018. doi:10.1029/2006GC001409.

Steinberger, B., Calderwood, A.R., 2006. Models of large-scale viscous flow in the Earth's mantle with constraints from mineral physics and surface observations. Geophys. J. Int. 167, 1461–1481. doi:10.1111/j.1365-246X.2006.03131.x.

Yuan, K., Beghein, C., 2013. Seismic anisotropy changes across upper mantle phase transitions. Earth Planet. Sci. Lett. 374, 132–144. doi:10.1016/j.epsl.2013.05.031.

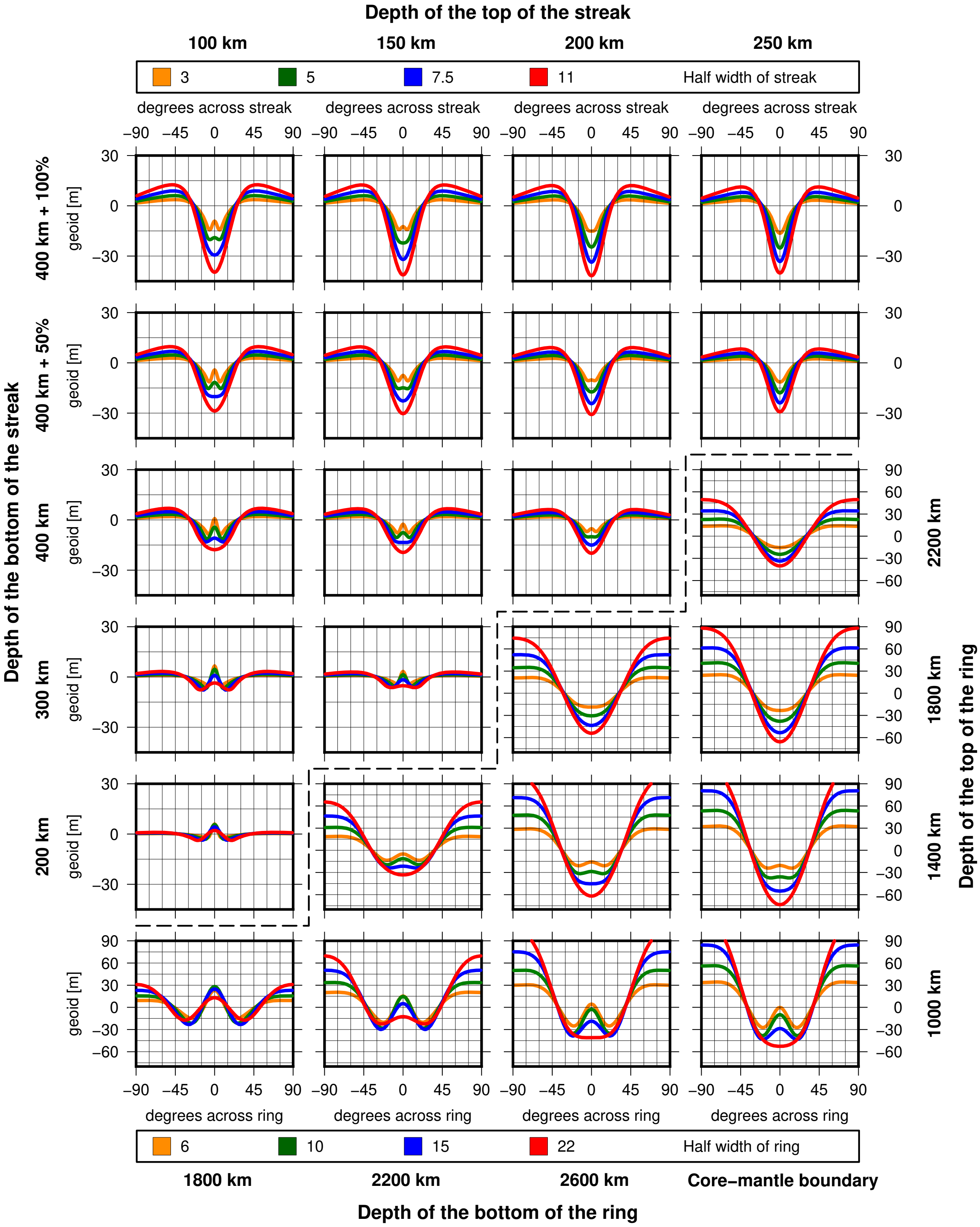

Figure 4: Dependence of the geoid on the width and depth range of a dense ring in the lower mantle along a profile across the ring (bottom right part below and to the right of dashed line) and of a low-density streak of length 96 degrees of arc in the upper mantle across the center of the streak (top left part above and to the left of dashed line). +50% means that half the effect of the phase transition (as in Figure 3) has been included, +100% means the full effect is included. Tapering as in Figure 3.

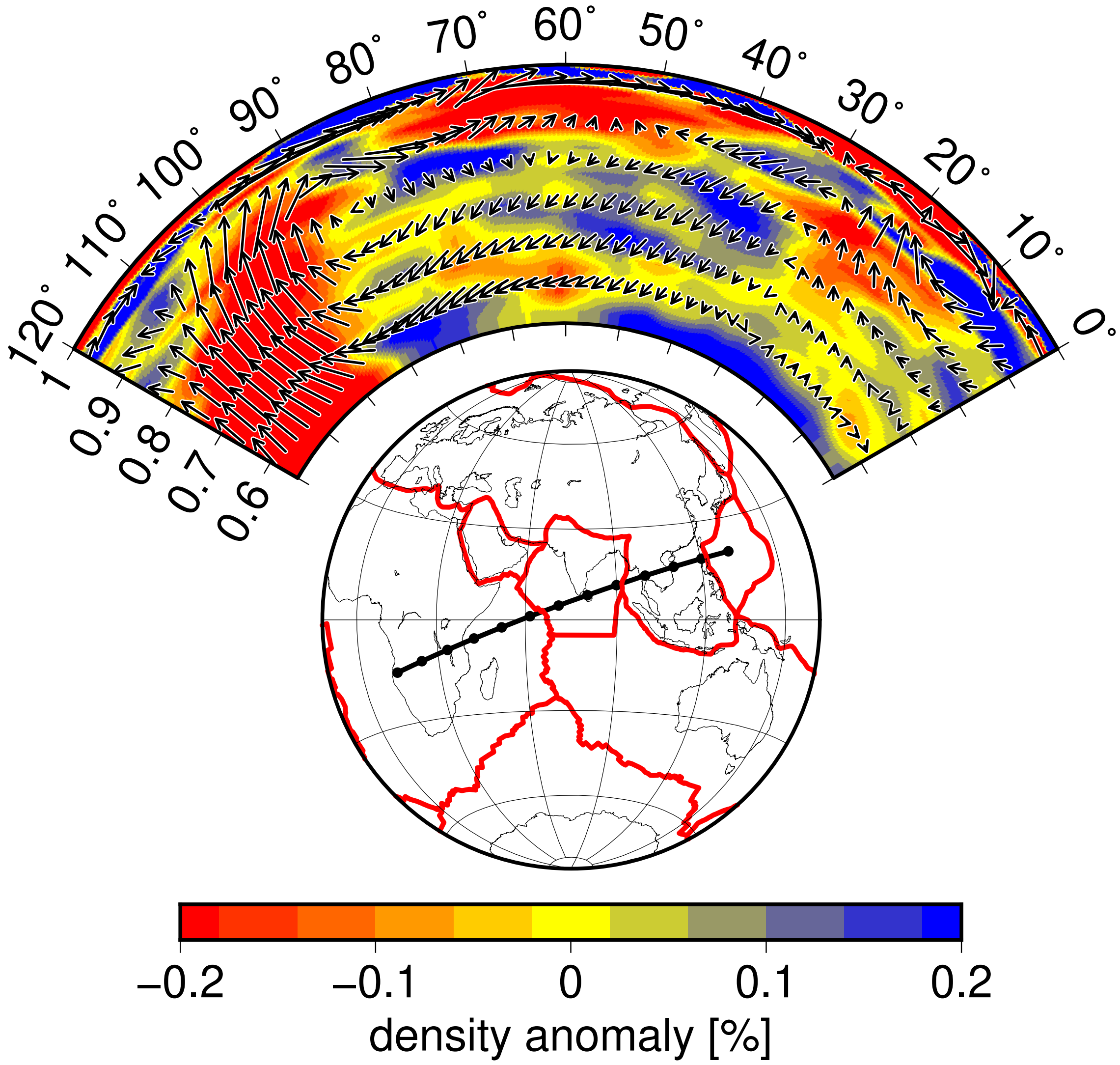

Figure 5: Vertical cross section through flow and density field for the reference model of Steinberger (2016).

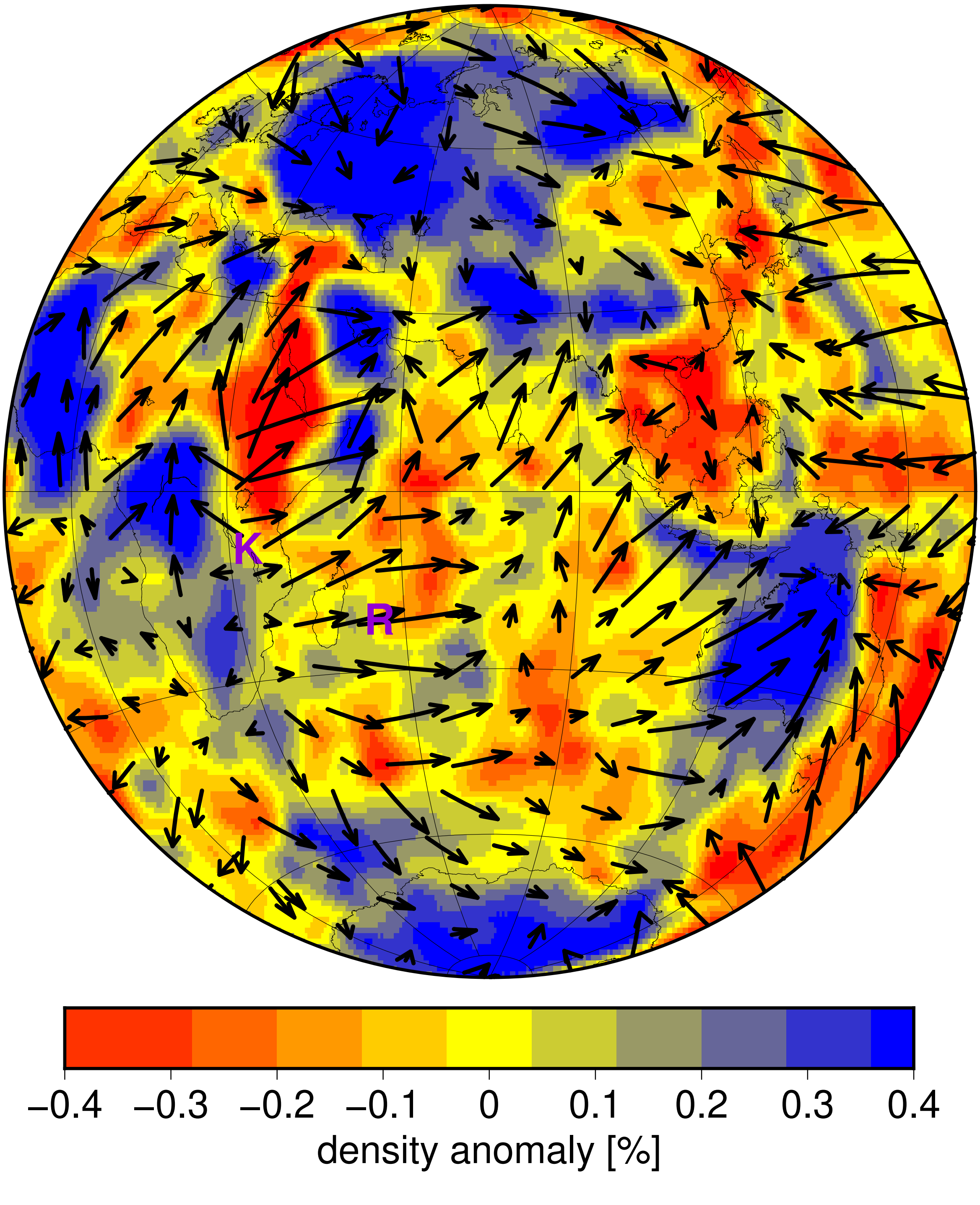

Figure 6: Average density anomaly in the depth range 100-400 km and flow field at depth 262.5 km for the reference model of Steinberger (2016). Letters K and R mark the Kenya and Réunion plumes, respectively.

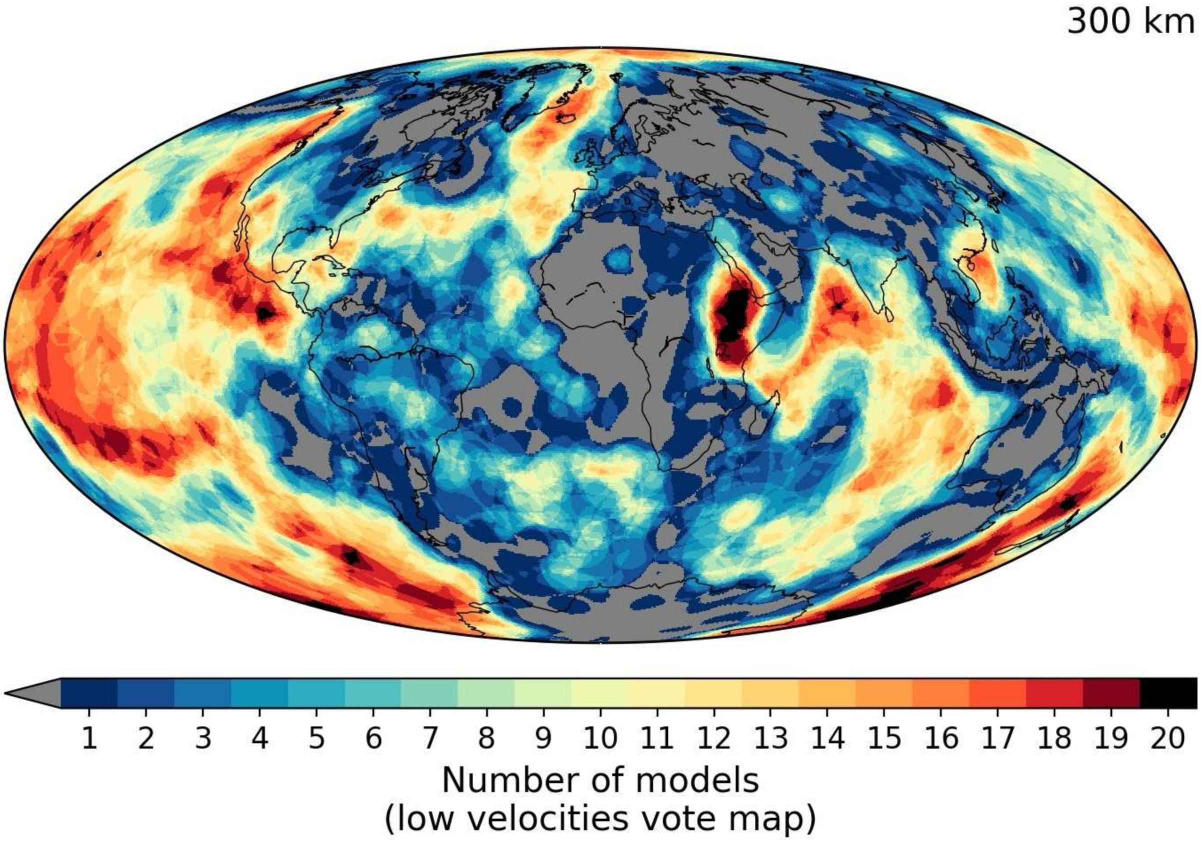

Figure 7: Votemap of all s-velocity models included by Hosseini et al. (2018) and |velocities| $\geq$ std.

Supplementary Material

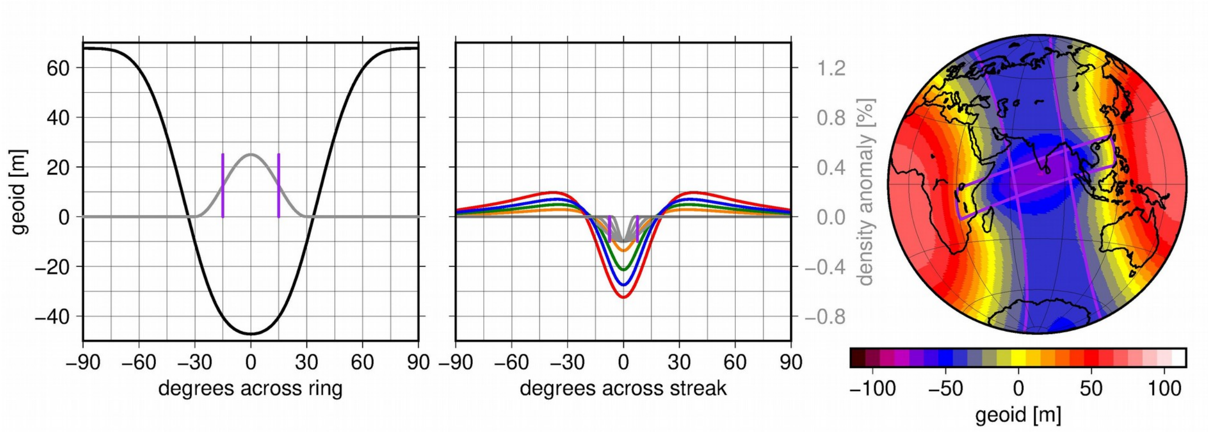

Figure S1: Modelled geoid map and profiles. As in Figure 3, but the low-density ``streak" is in the depth range 300 km to 900 km. The grey lines in the center panel show the density anomaly along a profile orthogonal to the streak across its centerpoint, with half-width 3°, 5°, 7.5° and 11°, and the orange (3°), green (5°), blue (7.5°) and red (11°) lines show the corresponding geoid height. The right panel shows a map view of the geoid from the density anomalies of the other two panels (streak width 7.5°) combined. It also shows as purple lines the outlines of the surface projection of both the ring and the streak (7.5° width), where the anomaly is 50% of its maximum, corresponding to the vertical purple lines in the left and center panels.

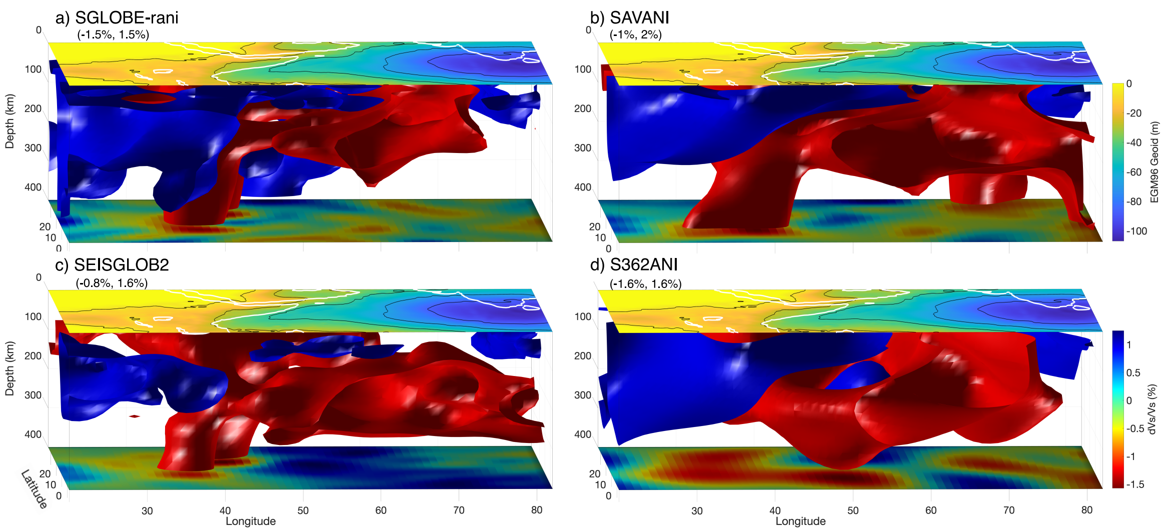

Figure S2: Isosurfaces of low- and high-velocity anomalies in the upper mantle beneath East Africa and the Indian Ocean from four global tomography models; SGLOBE-rani (Chang et al., 2015), SAVANI (Auer et al., 2014), SEISGLOB2 (Durand et al., 2017) and S36ANI (Kustowski et al., 2008). We used different values for isosurfaces in each model to clearly show the lowest-velocity anomalies, which are noted on the top left of each subplot. The top and bottom plane of each sub-figure shows the geoid based on the EGM96 geopotential model (Lemoine et al., 1998) and perturbations in isotropic shear wave speed, dVs/Vs (%) at 400 km depth, respectively. Contours are shown from -107 m every 20 m on the top plane of each sub-figure in black.

Supplementary References

Auer, L., Boschi, L., Becker, T.W., Nissen-Meyer, T., Giardini, D., 2014. Savani: A variable resolution whole-mantle model of anisotropic shear velocity variations based on multiple data sets. J. Geophys. Res. 119, 3006–3034. https://doi.org/10.1002/2013JB010773.

Chang, S.J., Ferreira, A.M.G., Ritsema, J., van Heijst, H.J., Woodhouse, J.H., 2015. Joint inversion for global isotropic and radially anisotropic mantle structure including crustal thickness perturbations. J. Geophys. Res. 120, 4278–4300. https://doi.org/10.1002/2014JB011824.

Durand, S., Debayle, E., Ricard, Y., Zaroli, C., Lambotte, S., 2017. Confirmation of a change in the global shear velocity pattern at around 1000 km depth. Geophys. J. Int. 211, 1628–1639. https://doi.org/10.1093/gji/ggx405.

Kustowski, B., Ekström, G., Dziewoński, A.M., 2008. Anisotropic shear-wave velocity structure of the Earth’s mantle: A global model. J. Geophys. Res. 113, B06306. https://doi.org/10.1029/2007JB005169.

Lemoine, F.G., Kenyon, S.C., Factor, J.K., Trimmer, R.G., Pavlis, N.K., Chinn, D.S., Cox, C.M., Klosko, S.M., Luthcke, S.B., Torrence, M.H., Wang, Y.M., Williamson, R.G., Pavlis, E.C., Rapp, R.H., Olson, T.R., 1998. The Development of the Joint NASA GSFC and the National Imagery and Mapping Agency (NIMA) Geopotential Model EGM96. Technical Report TP-1998-206861. NASA.